Ultra-Low Clouds over the Southern West African Monsoon Region

Note: This is the accepted version of the article. Some editorial changes may have been made before publication in GRL. This PDF also contains the auxiliary material. The correct citation is:

Knippertz P., A. H. Fink, R. Schuster, J. Trentmann, and C. Yorke, 2011: Ultra-Low Clouds over the Southern West African Monsoon Region. Geophys. Res. Lett., 38, L21808, doi:10.1029/2011GL049278.

Peter Knippertz

School of Earth & Environment, University of Leeds, Leeds LS2 9JT, UK

Andreas H. Fink, Robert Schuster

Institute for Geophysics and Meteorology, University of Cologne, Kerpener Str. 13, 50923 Köln, Germany

Jörg Trentmann

Satellite Application Facility on Climate Monitoring, German Weather Service, Frankfurter Straße 135, 63067 Offenbach, Germany

Jon M. Schrage

Department of Atmospheric Sciences, Creighton University, 2500 California Plaza, Omaha, NE 68178, USA

Charles Yorke

Ghana Meteorological Agency, P.O. Box LE 87, Legon, Accra, Ghana

Corresponding author: Peter Knippertz (p.knippertz@leeds.ac.uk)

Abstract

New ground- and space-based observations show that summertime southern West Africa is frequently affected by an extended cover of shallow, non-precipitating clouds only few hundred meters above the ground. These clouds are associated with nocturnal low-level wind speed maxima and frequently persist into the day, considerably reducing surface solar radiation. While the involved phenomena are well represented in re-analysis data, climate models show large errors in low-level wind, cloudiness, and solar radiation of up to 90 W m^{-2}. Errors of such a magnitude could strongly affect the regional energy and moisture budgets, which might help to explain the notorious difficulties of many models to simulate the West African climate. More effort is needed in the future to improve the monitoring, modeling, and physical understanding of these ultra-low clouds and their importance for the West African monsoon system.

1. Background

The West African monsoon (WAM) system involves multi-scale interactions between the atmosphere, the ocean, and the land surface. WAM variations affect remote regions such as the North Atlantic, Europe, India, and the tropical Pacific [*Cassou et al.*, 2005*; Losada et al.*, 2010; *Rodríguez-Fonseca et al.,* 2010*; Gaetani et al.*, 2011]. Climate models show large latitudinal biases of the main rain belt [*Cook and Vizy*, 2006] and disagree about the sign of precipitation change for the 21st century [*Christensen et al.*, 2007*; Druyan*, 2010; *Paeth et al.*, 2011]. This uncertainty hinders the development of adaptation strategies for one of the most vulnerable regions worldwide [*Boko et al.*, 2007]. Recent observational, diagnostic, and modeling work has concentrated on the spatio-temporal variability and dynamics of rainfalls over the Sahel, and on external drivers such as sea-surface temperatures, land surface processes, and aerosols [*Lafore et al.,* 2010; *Xue and Ruti*, 2010]. Here we use new ground- and space-based observations to show that the frequent occurrence of extended, shallow, ultra-low, non-precipitating stratiform clouds, which form in association with nocturnal low-level wind speed maxima, considerably reduce surface solar radiation over summertime southern West Africa. These clouds have so far received little attention [*Schrage et al.,* 2006; *Schrage and Fink*, 2010] in contrast to their oceanic counterparts [*Albrecht et al.,* 1995] and their role for the whole WAM system is unknown.

2. Data

To monitor low-level cloudiness, wind speed, and solar radiation over West Africa a wide range of space- and surface based observations have been used. The former include false-color composites from three infrared (IR) channels from Meteosat Second Generation (MSG), lidar backscatter coefficients from CALIPSO (Cloud-Aerosol Lidar and Infrared Pathfinder Satellite Observations; http://eosweb.larc.nasa.gov/PRODOCS/calipso/ table_calipso.html) and radar reflectivity from CloudSat (http://cloudsat.cira.colostate.edu/) [*Stephens et al.*, 2002]. In addition, more derived products such as surface solar irradiance from the Global Energy and Water Cycle Experiment Surface Radiation Budget (GEWEX-SRB) Project [*Stackhouse et al.*, 2011] and low-level cloud cover from the widely used International Satellite Cloud Climatology Project (ISCCP; see http://isccp.giss.nasa.gov) dataset [*Rossow and Schiffer*, 1999] were used. The three-hourly (monthly) ISCCP D1 (D2) product provides fractional cloud cover for levels below 800 hPa (680 hPa). Ground-based measurements include standard surface SYNOPs and METARs (in particular from Kumasi, Ghana) [*WMO*, 1995], pyranometer measurements of surface solar irradiance at Ilorin (Nigeria), Cotonou, Parakou (both Benin), and Kumasi (Ghana) as well as measurements with an ultra-high frequency profiler [*Lothon et al.*, 2008] and a ceilometer [*Pospichal and Crewell*, 2007] at Djougou (central Benin) deployed during the African Monsoon Multidisciplinary Analysis (AMMA) field campaign in 2006. Wind profiles are taken from 3-hourly radiosondes launched during AMMA, when several new stations were established, allowing for the first time a reliable estimate of the diurnal cycle at the regional scale [*Parker et al.*, 2008]. Here we use all available data from the four stations Abuja (Nigeria), Cotonou, Parakou (both Benin), and Tamale (Ghana).

As a near-observational modeling reference, short-term forecasts started at 0000 UTC every day made in the production of the European Centre for Medium-Range Weather Forecasts (ECMWF) ERA Interim re-analyses [*Dee et al.*, 2011] covering the period 1989–2010 were used on standard pressure levels with a horizontal resolution of 0.5°. The advantages of using short-term forecasts are (i) a 3-hourly time resolution (in contrast to 6-hourly for the actual re-analysis data) and (ii) a physically consistent diurnal cycle using the model forecast times +3h to +24h. Since solar irradiance data are not assimilated, differences between short-term model forecasts and the actual re-analysis are small (not shown). To assess state-of-the-art climate models the World Climate Research Programme's (WCRP's) Coupled Model Intercomparison Project phase 3 (CMIP3) multi-model dataset [*Meehl et al.*, 2007] was used. The analysis concentrates on the period 1961–1999 from the “climate of the 20th Century experiments (20C3M)”, which were initialized in the pre-industrial control runs. More details on the data used in this paper including a map with all station locations are provided in the Auxiliary Material. All analyses concentrate on the time of the peak summer monsoon July–September and on the geographical region 6–10°N, 7°W–7°E (see black boxes in Figures 2–4).

3. An Example

Figure 1 provides an example of a night with a clear view on an extended cover of low-level stratus over southern West Africa and demonstrates the challenge to observe these with the existing network. MSG IR composites and corresponding human-eye observations agree well on the extent of the cloud deck (Figure 1a). The ISCCP retrieval, however, reveals a dramatic underestimation, mostly likely caused by the small IR contrast to the surface (Figure 1b). A vertical cross section from the CALIPSO lidar (Figure 1c) clearly shows low clouds over southern Nigeria, which are obscured by ground clutter in a corresponding CloudSat radar profile (Figure 1d). Before the new capabilities of MSG and CALIPSO nocturnal low-level clouds were mainly observed by eye from the ground. This is still true today in the presence of elevated layers of cloud and/or aerosol. Measurements with a ceilometer at Djougou (Benin) reveal the extremely low base of the cloud deck over this location, which descends to the surface in the course of the night and then rises and breaks open around noon (Figure 1e). Collocated wind measurements (Figure 1f) show a prominent nighttime maximum in the monsoonal southerlies, often referred to as a nocturnal low-level jet (NLLJ) [*Parker et al.*, 2005; *Lothon et al.*, 2008]. This suggests that shear-induced turbulence below the jet core mixes moist air from the surface upward to create the cloud deck [*Bonner and Winninghoff,* 1969].

4. Observational Climatologies

Recently available longer-term climatologies of clouds and winds confirm these ideas. The summer mean diurnal cycle of low-cloud cover from Kumasi airport (Ghana; Figure 2a) reveals a distinct diurnal cycle with a sharp increase shortly after sunset, a maximum around 75% at sunrise, a slow decrease until the early afternoon, followed by a steep drop below 30% at 2000 UTC. A decrease in cloudiness between morning and early afternoon is also seen in the visible channel of the Moderate Resolution Imaging Spectroradiometer MODIS [*Douglas et al.*, 2010]. ISCCP data largely underestimate low-level cloudiness across large parts of southern West Africa (Figure 2b) and show a reversal of the diurnal cycle (Figure 2a, see also Auxiliary Figure S3). Averaged wind profiles from four radiosondes stations clearly show the NLLJ with maximum wind speeds of ~7 m s^{-1} at 0300 and 0600 UTC and weaker winds during the afternoon (Figure 2c). A second peak of about 8 m s^{-1} is observed at about 680 hPa, possibly to do with the southern flank of the midlevel African Easterly Jet (AEJ). The close correspondence between the diurnal cycles of wind and clouds support the idea of NLLJ-induced mixing of moisture. The persistence of the clouds after sunrise, together with large albedo differences to the underlying lush vegetation (0.9 vs. 0.15), substantially reduces surface incoming solar radiation. Ground observations show summer means as low as 147 W m^{-2} with values increasing towards the Sahel (Figure 2d). The high value of 198 W m^{-2} at Cotonou is most likely only representative of a narrow coastal strip, where the passage of the sea-breeze front in the morning and upwelling of cooler waters along parts of the coastline support clearer skies.

GEWEX satellite retrievals (Figure 2d) show a broad local minimum over southern West Africa with an average of 178.5 W m^{-2} over the box marked in black in Figure 2d (which represents the mostly flat areas away from the Guinean Highlands, the Jos Plateau, and the Cameroon Mountains, see Figure S1 in the Auxiliary Material). The ground observations suggest a slight positive bias in the GEWEX data, potentially related to cloud-detection problems in the morning and evening hours. Other satellite retrievals have larger positive biases (Auxiliary Table S1 and Figures S5 and S6).

Horizontal distributions of low-level cloudiness from the ECMWF ERA-Interim re-analysis (Figure 3a) show a clear maximum over the whole of southern West Africa with particularly high values over orographic features. The regional average of 59% and its diurnal cycle are in good agreement with the observations at Kumasi (Figures 2a and 3a). Vertical profiles of model layer cloud cover (Figure 3b) confirm the gradual spreading of low stratus clouds in the course of the night. After sunrise, the peak in cloudiness broadens vertically and rises to 800 hPa until 1500 UTC. Smallest cloud covers are found at 1800 and 2100 UTC. Above 700 hPa, cloudiness shows a negligible diurnal cycle with a mean cover < 10%. Vertical profiles of wind speed (Figure 3c) also show a strong diurnal cycle in good agreement with radiosonde data (Figure 2c). The slightly weaker mean 925 hPa wind speed of 5.3 m s^{-1} in ERA-Interim compared to 5.8 m s^{-1} in the radiosonde data is most likely due to the coastal station Cotonou with its unrepresentatively high wind speeds (Auxiliary Figure S4). The midlevel maximum is slightly higher in ERA-Interim, possibly due to few stations close to the AEJ core in the north of the region. Solar irradiance estimates (Figure 3d) show a close correspondence to the low cloud cover (Figure 3a) and a good agreement with the station observations with a regional average of 161.3 W m^{-2}.

5. Climate Models

Long-term mean profiles from the CMIP3 multi-model dataset show a general underestimation of low-level clouds and an overestimation of mid-level clouds (Figure 4a) with respect to ERA-Interim. The diversity between models is immense in both cloud amounts and vertical distribution with few showing profiles similar to the re-analysis. Daily mean wind profiles also show considerable variations with many models overestimating NLLJs by almost a factor of 2 with respect to observations (Figure 4b). The problems of representing low (and also midlevel) clouds evident from Figure 4a lead to a massive overestimation of surface solar irradiance over southern West Africa (Figure 4c). The regional average of 190.2 W m^{-2} is almost 30 W m^{-2} larger than that of ERA-Interim with individual models deviating by as much as 98 W m^{-2} (Auxiliary Table S2). All ERA-Interim–CMIP3 model differences are statistically significant on at least the 95% level. Pertinent inter-model standard deviations indicate a maximum disagreement over southern West Africa, particularly over high terrain and the west coast (Figure 4d), with a regional average of 39.4 W m^{-2}. This bias and uncertainty in solar energy input can be expected to influence the surface energy budget, low-level temperature, and pressure, and possibly the entire monsoon circulation [*Eltahir and Gong*, 1996]. Future research should investigate to what extent these deficits influence the overall model performance for the WAM. Differences between individual models are one order of magnitude larger than typical differences between simulations with or without ocean coupling, and between current and future climates of the same model (Auxiliary Figure S7), making reliable climate-change projections practically impossible.

6. Discussion and Conclusions

Recently available ground- and space-based observations and short-term ECMWF forecasts have been analyzed to better document and understand the climatology of low-level cloudiness over summertime West Africa. Based on this the following mechanism is suggested [see also *Bonner and Winninghoff*, 1969; *Schrage et al.*, 2006; *Schrage and Fink*, 2010]: (I) Around sunset, mixing in the planetary boundary layer breaks down followed by a minimum in cloudiness. (II) Radiative cooling stabilizes a shallow surface layer, where winds slacken and moisture accumulates through evapotranspiration. (III) Due to decoupling from surface friction winds accelerate above the weak surface inversion (few hundred meters above ground) in response to the monsoonal north–south pressure gradient, forming a NLLJ. (IV) Increasing vertical wind shear below the jet mechanically generates turbulence, which mixes moist surface air upwards and leads to the formation of ultra-low clouds. (V) Some nights show several mixing cycles with intermittent turbulence until increased downwelling longwave radiation from the thickened cloud deck stops further cooling of the surface. This creates a positive feedback leading to the predominance of fully overcast nights over southern West Africa during summer (Auxiliary Figure S2). (VI) It can take until the early afternoon for solar heating to fully erode the NLLJ and cloud deck, which is then often replaced by fair-weather cumuli.

While observations and ECMWF data show an overall satisfactory agreement, CMIP3 climate models tend to show too strong winds and too little cloud cover at low levels. A possible explanation for these biases is too little vertical mixing in the stable nighttime boundary layer, leading to too much decoupling from the surface and thus a reduced upward transport of surface moisture and a too weak deceleration the NLLJ through surface friction. The formation of fog in some models in Figure 4a (e.g. cccma) supports this hypothesis. It is conceivable that the atmospheric moisture budget, especially moisture recycling from vegetation and the low-level northward transport, is also adversely affected by these biases. A possible reason could be insufficient temporal and vertical resolution. The former might cause models to miss out on the first onset of stratus leading to too much radiative cooling and decoupling through positive feedbacks [*Schrage et al.*, 2006]. The latter might not allow models to represent the downward propagation of shear-induced turbulence from underneath the NLLJ core to the surface [*Bain et al.*, 2010]. A comparison between the high- and medium-resolution version of the Miroc3 model (56 vs. 20 levels), however, shows similar overestimations of the NLLJ, but more realistic clouds at high resolution, indicating that other factors must play a role, too. Potentially important are feedbacks of the cloud evolution with the surface energy budget and hydrology, which influences relative humidity and stability. In the real atmosphere, subtle variations in low-level static stability and humidity, as well as in the background pressure gradient that drives the NLLJ, can decide between cloudy and clear nights [*Schrage et al.*, 2006; *Schrage and*

Fink, 2010]. Disentangling the details of the relationship between errors in the large-scale pressure and moisture distributions, clouds, winds, surface hydrology, and radiation in CMIP3 data is beyond the scope of this paper. However, the good representation of all features in the more constraint ECMWF model is encouraging and could serve as a benchmark to evaluate free-running climate models more rigorously, using output with higher temporal resolution to resolve the diurnal cycle and to conduct targeted sensitivity experiments. In parallel, more efforts are needed to improve the representation of low clouds in satellite retrievals for a better observational constraint on models. These, together with ground-based observations from AMMA and other initiatives, will help to build a more robust climatology and to advance our physical understanding of the controls of cloud formation. In the long run, it is hoped that this work will enhance our capability to model the WAM and make better projections of climate change over this crucial region.

Acknowledgments

We acknowledge funding from the German Science Foundation (KN 581/2-3) and for IMPETUS (BMBF Grant 01LW06001A, North Rhine-Westphalia Grant 313-21200200) and QWeCI (EU Grant 243964). The MSG, ceilometer, and wind profiler data (Figure 1) were obtained from the AMMA database and we acknowledge Bernhard Pospichal and Bernard Campistron, respectively. We thank the Kwame Nkrumah University of Science and Technology for supporting the Kumasi field site, the World Radiation Monitoring Center for radiation data from Ilorin, the NASA CloudSat project for CloudSat data, and the UK Met Office for providing access to ERA-Interim re-analyses. The GEWEX SRB and CALIPSO data were obtained from the NASA Langley Research Center Atmospheric

Sciences Data Center. We acknowledge the modeling groups, the Program for Climate Model Diagnosis and Intercomparison, and the WCRP's Working Group on Coupled Modelling for their roles in making available the WCRP CMIP3 multi-model dataset, support of which is provided by the Office of Science, U.S. Department of Energy. We would also like to thank two anonymous reviewers for their helpful comments.

References

Albrecht, B. A., C. S. Bretherton, D. Johnson, W. H. Schubert, and A. S. Frisch (1995), The Atlantic Stratocumulus Transition Experiment – ASTEX, *Bull. Am. Meteorol. Soc.*, *76,* 889–904.

Bain, C. L., D. J. Parker, C. M. Taylor, L. Kergoat, and F. Guichard (2010), Observations of the nocturnal boundary layer associated with the West African Monsoon, *Mon. Wea. Rev., 138*, 3142–3156.

Boko, M., et al. (2007), Africa, in *Climate Change 2007: Impacts, adaptation and vulnerability. Contribution of Working Group II to the Fourth Assessment Report of the Intergovernmental Panel on Climate Chang*, edited by M. L. Parry, et al., pp. 433–467, Cambridge University Press, Cambridge, UK.

Bonner, W. D., and F. Winninghoff (1969), Satellite studies of clouds and cloud bands near the low-level jet, *Mon. Wea. Rev.*, *97,* 490–500.

Cassou, C., L. Terray, and A. S. Phillips (2005), Tropical Atlantic influence on European heatwaves, *J. Clim.*, *18,* 2805–2811.

Christensen, J. H., et al. (2007), Regional climate projections, in *Climate Change 2007: The physical science basis. Contribution of Working Group I to the Fourth Assessment*

Report of the Intergovernmental Panel on Climate Change, edited by S. Solomon, et al., pp. 847–940, Cambridge University Press, Cambridge, UK and New York, NY, USA.

Cook, K. H., and E. K. Vizy (2006), Coupled model simulations of the West African monsoon system: 20th century simulations and 21st century predictions, *J. Clim., 19,* 3681–3703.

Dee, D. P., et al. (2011), The ERA-Interim reanalysis: configuration and performance of the data assimilation system, *Q. J. R. Meteorol. Soc.*, *137,* 553–597.

Douglas, M., R. Beida, and A. Dominguez (2010), Developing high spatial resolution daytime cloud climatologies for Africa, paper presented at 29th Conference on Hurricanes and Tropical Meteorology, Tucson, AZ.

Druyan, L. M. (2010), Studies of 21st-century precipitation trends over West Africa, *Internat. J. Climatol.*, doi:10.1002/joc.2180.

Eltahir, E. A. B., and C. Gong (1996), Dynamics of the wet and dry years in West Africa, *J. Clim.*, *9*, 1030–1042.

Gaetani, M., B. Pohl, H. Douville, and B. Fontaine (2011), West African Monsoon influence on the summer Euro-Atlantic circulation, *Geophys. Res. Lett.*, *38,* L09705.

Lafore, J.-P., C. Flamant, V. Giraud, F. Guichard, P. Knippertz, J.-F. Mahfouf, P. Mascart, and E. R. Williams (2010), Introduction to the AMMA Special Issue on 'Advances in understanding atmospheric processes over West Africa through the AMMA field campaign, *Q. J. R. Meteorol. Soc.*, *136,* 2–7.

Losada, T., B. Rodríguez-Fonseca, I. Polo, S. Janicot, S. Gervois, F. Chauvin, and P. Ruti (2010), Tropical response to the equatorial mode: AGCM multimodel approach, *Clim. Dyn*., *35,* 45–52.

Lothon, M., F. Saïd, F. Lohou, and B. Campistron (2008), Observation of the diurnal cycle in the low troposphere of West Africa, *Mon. Wea. Rev., 136,* 3477–3500.

Meehl, G. A., C. Covey, T. Delworth, M. Latif, B. McAvaney, J. F. B. Mitchell, R. J. Stouffer, and K. E. Taylor (2007), The WCRP CMIP3 multi-model dataset: A new era in climate change research, *Bull. Am. Meteorol. Soc., 88,* 1383–1394.

Paeth, H., et al. (2011), Progress in regional downscaling of West African precipitation, *Atmos. Sci. Lett.,* 12, 75–82.

Parker, D. J., R. R. Burton, A. Diongue-Niang, R. J. Ellis, M. Felton, C. M. Taylor, C. D. Thorncroft, P. Bessemoulin, and A. M. Tompkins (2005), The diurnal cycle of the West African monsoon circulation, *Q. J. R. Meteorol. Soc.,* 131, 2839–2860.

Parker, D. J., et al. (2008), The AMMA radiosonde program and its implications for the future of atmospheric monitoring over Africa, *Bull. Am. Meteorol. Soc., 89***,** 1015–1027.

Pospichal, B., and S. Crewell (2007), Boundary layer observations in West Africa using a novel microwave radiometer, *Meteorol. Z., 16(5),* 513–523.

Rodríguez-Fonseca, B., I. Polo, J. Garcia-Serrano, T. Losada, E. Mohino, C. R. Mechoso, and F. Kucharski (2009), Are Atlantic Niños enhancing Pacific ENSO events in recent decades?, *Geophys. Res. Lett., 36,* L20705, doi:10.1029/2009GL040048.

Rossow, W. B., and R. A. Schiffer (1999), Advances in understanding clouds from ISCCP, *Bull. Am. Meteorol. Soc., 80,* 2261–2288.

Schrage, J. M., S. Augustyn, and A. H. Fink (2006), Nocturnal Stratiform Cloudiness during the West African Monsoon, *Meteorol. Atmos. Phys., 95,* 73–86.

Schrage, J. M., and A. H. Fink (2010), A possible mechanism regulating nocturnal stratocumulus decks in West Africa, paper presented at 29th Conference on Hurricanes and Tropical Meteorology, Tucson, AZ.

Stackhouse Jr., P. W., S. K. Gupta, S. J. Cox, T. Zhang, J. C. Mikovitz, and L. M. Hinkelman (2011), 24.5-year SRB data set released, *GEWEX News, 21(1),* 10–12.

Stephens, G., et al. (2002), The Cloudsat mission and the A-train, *Bull. Am. Meteorol. Soc., 83,* 1771–1790.

World Meteorological Organization (1995), *Manual on codes. International Codes, Vol. I.1, Part A—Alphanumeric Codes*. WMO-No. 306, World Meteorological Organization, Geneva, Switzerland.

Xue, Y., and P. M. Ruti, (2010), Prelude to Special Issue: West African monsoon and its modeling, *Clim. Dyn., 35*, 1–2.

Figure Captions

Figure 1. Example case 20 August 2006. (a) MSG IR composite at 0130 UTC on (low clouds in green) with 0300 UTC ground observations of low-cloud cover in octas as symbols. (b) ISCCP 3-hourly mean low-cloud cover centered on 0000 UTC. (c) and (d) Vertical profiles at 0130 UTC and orography along the track shown in (A) from the CALIPSO lidar and CloudSat radar. (e) and (f) 1600 UTC 19 – 1600 UTC 20 August observations of clouds and winds from a ceilometer and a ultra-high frequency profiler at Djougou (central Benin).

Figure 2. Summer climatologies from observations. (a) Mean diurnal cycle of low-cloud cover from eye observations at Kumasi airport (Ghana; 2010 only), and regional averages from ERA-Interim (1989–2010, see Figure 3) and ISCCP D2 (1983–2007). (b) Corresponding horizontal distribution from ISCCP D2 with the 60% observations from Kumasi marked, both averaged over the diurnal cycle and the same years as in (a). (c) Mean diurnal cycle of vertical profiles of wind speed from the radiosonde stations Abuja, Cotonou, Parakou, and Tamale during 2006 (mean in blue). (d) Solar irradiance at the surface from GEWEX satellite data 1983–2007 and the four ground stations Ilorin, Cotonou, Parakou, and Kumasi as numbers (observation periods are given in the Auxiliary Material). All means are calculated from available July–September observations. Black boxes mark the area used for spatial averaging (6–10°N, 7°W–7°E).

Figure 3. Summer climatologies from ERA-Interim re-analysis short-term forecasts. (a) Daily mean low-level cloud cover [%]. (b) and (c) Regionally averaged diurnal cycles of vertical profiles of layer cloud cover and wind speed, respectively (means in black). (d) Solar irradiance at the surface. All means are calculated from July–September 1989–2010. Black boxes and observations from ground stations are as in Figure 2.

Figure 4. Summer climatologies from the CMIP3 multi-model dataset. (a) and (b) Regionally averaged daily mean vertical profiles of layer cloud cover (16 models; ERA-Interim mean in black) and wind speed (20 models with mean dashed; solid black line is calculated from daily averages of the zonal and meridional wind component from ERA-Interim data; models with asterisk have monthly data only). (c) Mean and (d) standard

deviation of solar irradiance at the surface (19 models). All CMIP3 model values are calculated from July–September 1961–1999. Black boxes are as in Figures 2 and 3.

Figures

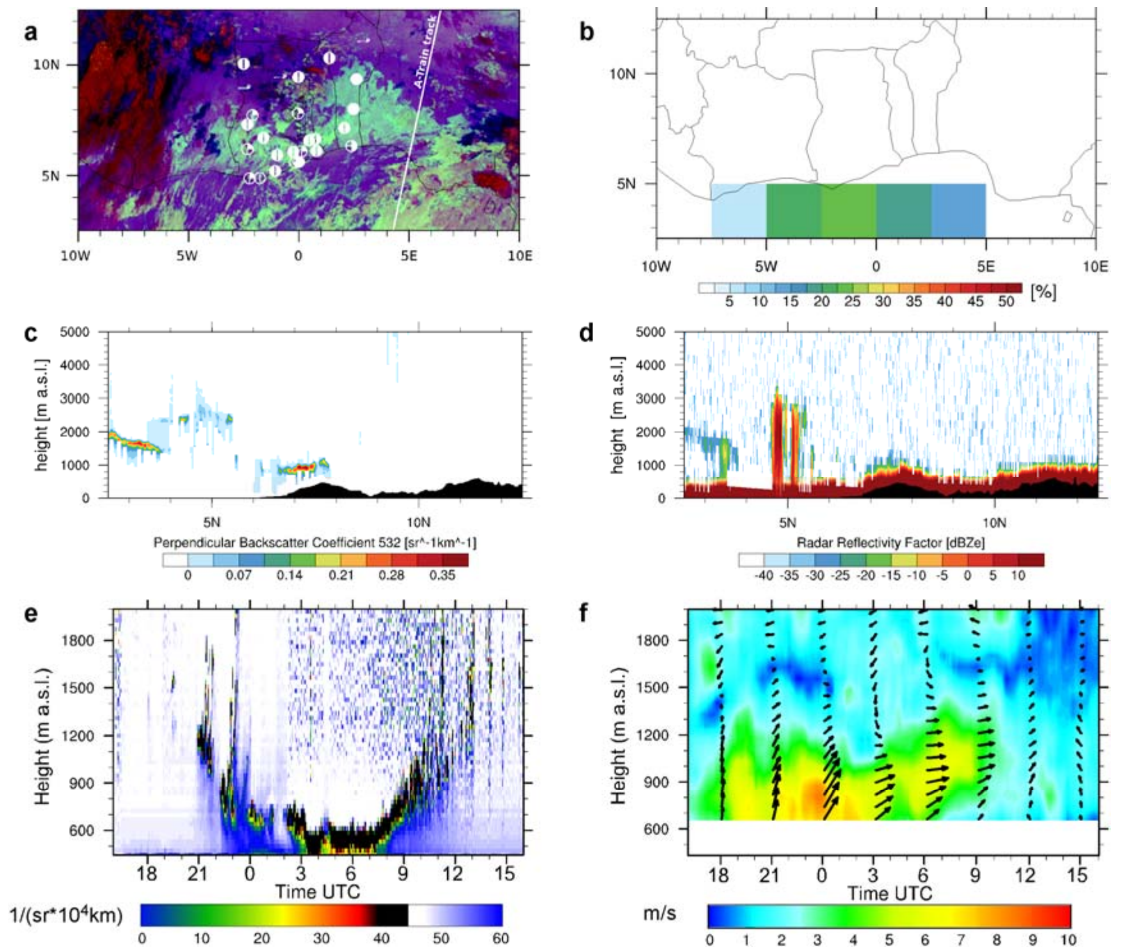

Figure 1. Example case 20 August 2006. (a) MSG IR composite at 0130 UTC on (low clouds in green) with 0300 UTC ground observations of low-cloud cover in octas as symbols. (b) ISCCP 3-hourly mean low-cloud cover centered on 0000 UTC. (c) and (d) Vertical profiles at 0130 UTC and orography along the track shown in (A) from the CALIPSO lidar and CloudSat radar. (e) and (f) 1600 UTC 19 – 1600 UTC 20 August observations of clouds and winds from a ceilometer and a ultra-high frequency profiler at Djougou (central Benin).

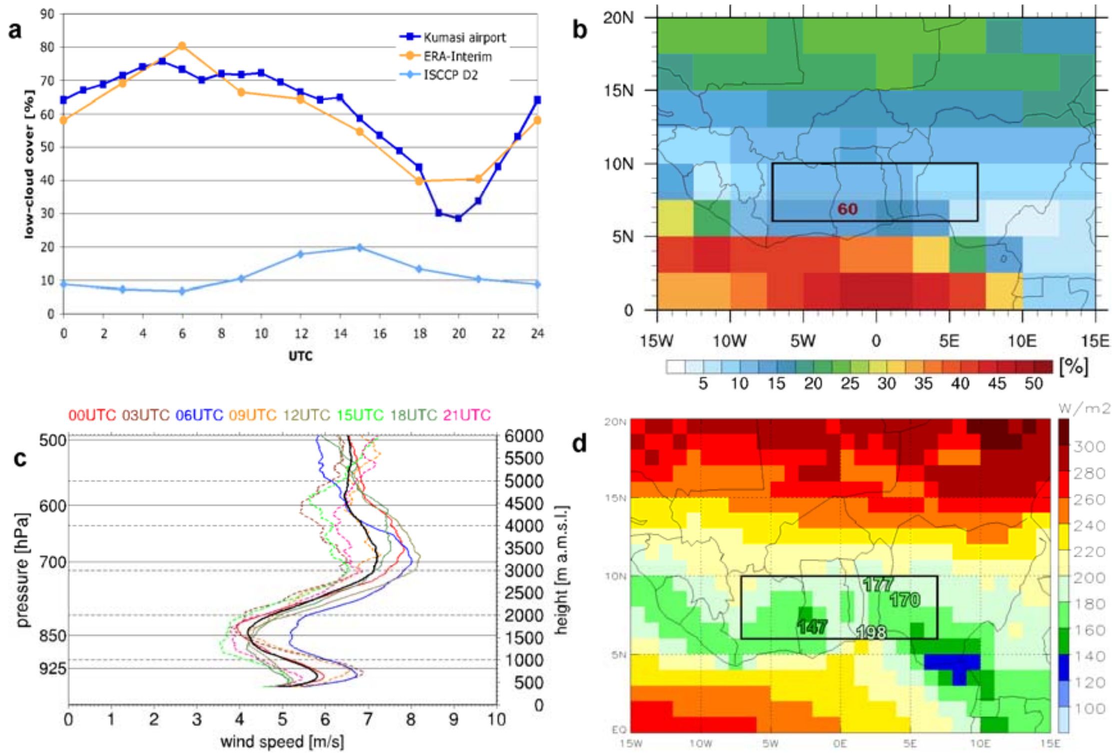

Figure 2. Summer climatologies from observations. (a) Mean diurnal cycle of low-cloud cover from eye observations at Kumasi airport (Ghana; 2010 only), and regional averages from ERA-Interim (1989–2010, see Figure 3) and ISCCP D2 (1983–2007). (b) Corresponding horizontal distribution from ISCCP D2 with the 60% observations from Kumasi marked, both averaged over the diurnal cycle and the same years as in (a). (c) Mean diurnal cycle of vertical profiles of wind speed from the radiosonde stations Abuja, Cotonou, Parakou, and Tamale during 2006 (mean in blue). (d) Solar irradiance at the surface from GEWEX satellite data 1983–2007 and the four ground stations Ilorin, Cotonou, Parakou, and Kumasi as numbers (observation periods are given in the Auxiliary Material). All means are calculated from available July–September observations. Black boxes mark the area used for spatial averaging (6–10°N, 7°W–7°E).

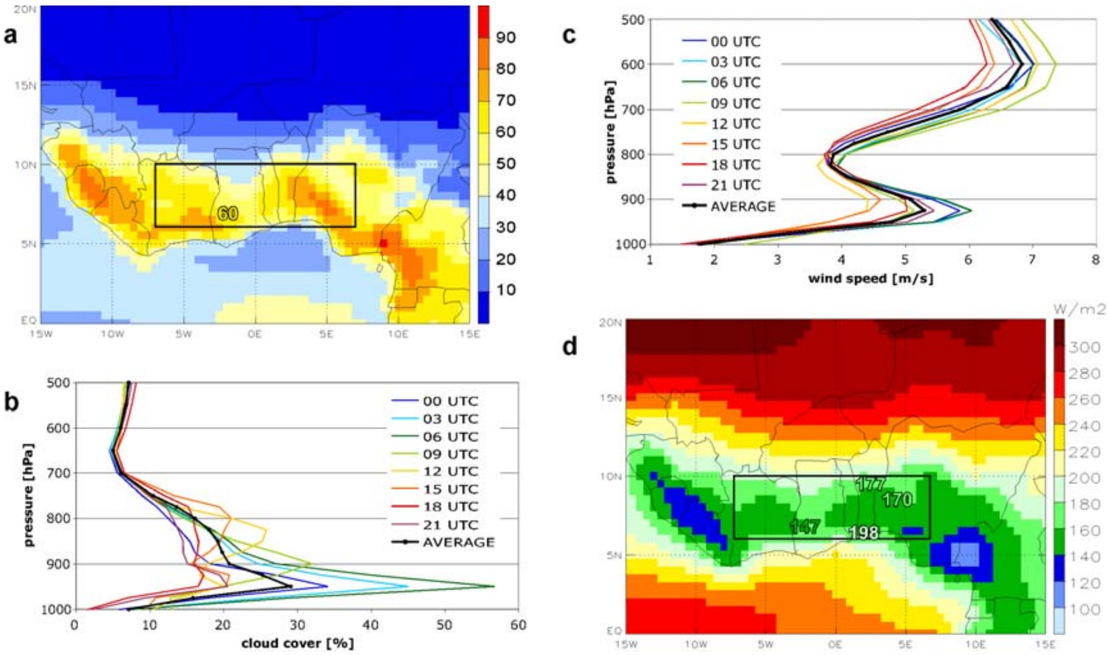

Figure 3. Summer climatologies from ERA-Interim re-analysis short-term forecasts. (a) Daily mean low-level cloud cover [%]. (b) and (c) Regionally averaged diurnal cycles of vertical profiles of layer cloud cover and wind speed, respectively (means in black). (d) Solar irradiance at the surface. All means are calculated from July–September 1989–2010. Black boxes and observations from ground stations are as in Figure 2.

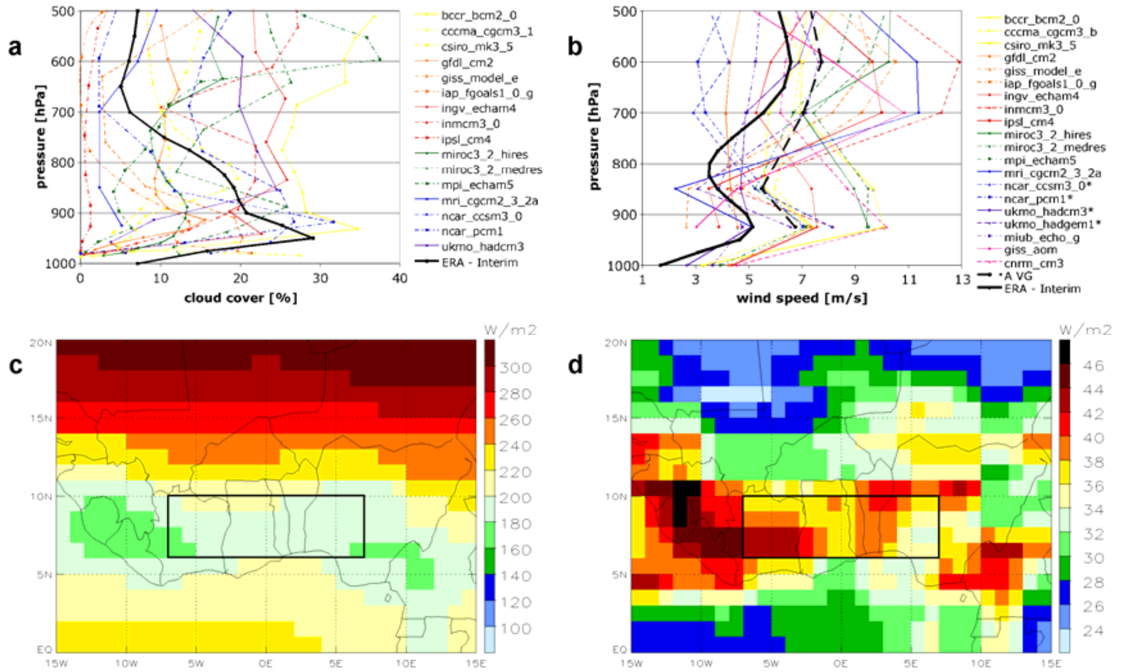

Figure 4. Summer climatologies from the CMIP3 multi-model dataset. (a) and (b) Regionally averaged daily mean vertical profiles of layer cloud cover (16 models; ERA-Interim mean in black) and wind speed (20 models with mean dashed; solid black line is calculated from daily averages of the zonal and meridional wind component from ERA-Interim data; models with asterisk have monthly data only). (c) Mean and (d) standard deviation of solar irradiance at the surface (19 models). All CMIP3 model values are calculated from July–September 1961–1999. Black boxes are as in Figures 2 and 3.

Ultra-Low Clouds over the Southern West Africa Monsoon Region

by *P. Knippertz, A. H. Fink, R. Schuster, J. Trentmann, J. M. Schrage & C. Yorke*

– Auxiliary Material –

1. Introduction

The purpose of this supplementary information is to provide details on the data used for the main paper. It is structured as follows: The first three sections discuss the data used to monitor low-level clouds (Section 2), low-level wind (Section 3), and solar irradiance (Section 4). Section 5 provides information on the gridded model datasets (ERA-Interim and CMIP3 data) as well as the procedure used to bring these datasets on a common latitude-longitude grid.

2. Monitoring of low-level clouds

(a) Ground-based

Most synoptic weather stations across West Africa (see Figure S1 for locations) are manned and operational 24 hours a day. The trained observers report eye observations of cloudiness on an hourly basis according to World Meteorological Organisation (WMO) regulations. These cloudiness reports are transmitted into the Global Telecommunication Network (GTS) of the WMO on a 3- or 6-hourly basis. Cloud information (i.e., cloud types, cloud cover in octas, and height of cloud base above ground level) is coded in parts I and III of the WMO FM12 SYNOP code [*WMO*, 1995] (see also http://www.wmo.int/pages/prog/www/ WMOCodes.html). Cover of low clouds (or if not present mid-level clouds) and types of low-, mid-, and high-level clouds are provided in the

8th group of part I in the SYNOP code. More details on cloudiness are given in the 8th group of part III with multiple occurrences of this group in cases of various cloud types present. This way, it is possible, for example, to distinguish between cumulus and stratocumulus cloud characteristics, although they have a common code (i.e., C_L=8) in the first part of the SYNOP. Hourly cloud information from part III of the SYNOP code from Kumasi (see Figure S1 for location) was used to produce Figures 1a and 2a of the main paper.

Figure S2 shows a climatological analysis of SYNOP cloud information for 0600 UTC reports during July–September 2006, which gives clear evidence of frequent low-cloud decks. To produce this figure data from part III of the SYNOP was used and only 8th groups with C_L= 6 (stratus, St) and C_L= 7 (stratocumulus, Sc) coding were considered. Some data gaps for Ghana were filled with information from part I of the SYNOP. Figure S2a shows the frequency of occurrence of stratus. Several stations along and to the north of the Guinea Coast report stratus almost every day at 0600 UTC. Less frequent occurrences are found to the north of about 9°N. The largest coverage of stratus, however, is observed away from the coast, where many stations report a mean stratiform cloud coverage of 5.5–7.5 octas. Keeping in mind the problems of cloud observations from space (see main paper), this example shows that human-eye cloud observations are valuable to document the extensive, low-level stratus decks over West Africa, even though the network suffers from frequent data gaps. In this case data provisions from the archives of the Meteorological services of Ghana and Benin led to a reporting frequency of 100% for these countries. Another source of information, which was available in 2006 only, is the ceilometer data from Djougou shown in Figure 1e of the main paper (see Figure S1 for station location).

(b) Satellites

A widely used cloud product is the International Satellite Cloud Climatology Project (ISCCP) dataset [*Rossow and Schiffer*, 1999]. The three-hourly ISCCP D1 product provides information of cloud cover for levels below 800 hPa and was used for Figure 1b of the main paper. The monthly ISCCP D2 product was used to generate Figures 2a and 2b of the main paper and provides coverage of clouds below 680 hPa. Both datasets were obtained from the ISCCP web site http://isccp.giss.nasa.gov maintained by the ISCCP research group at the NASA Goddard Institute for Space Studies, New York, NY. Figure S3 shows the mean diurnal cycle of this product for southern West Africa. The data suggest continuous high cloud amounts over the tropical Atlantic and a daytime maximum of low clouds over the Sahel. The shallow ultra-low clouds over southern West Africa are hardly detected at all with a weak maximum at 1500 UTC in strong contrast to observations. The most likely explanation for this behavior is the small contrast in the infrared signal between these clouds and the underlying surface. More information on ISCCP can be found in Section 4b below.

A qualitative way to visualize the low stratiform clouds over West Africa at night are Meteosat Second Generation (MSG) false-color images produced from a combination of brightness temperatures from three SEVIRI (Spinning Enhanced Visible and Infrared Imager) infrared channels with: blue = channel 9 (10.8 μm); red = channel 10 (12 μm) minus channel 9; green = channel 9 minus channel 4 (3.9 μm). Such an image is shown as Figure 1a of the main paper with the low-level stratus deck clearly standing out in greenish colors. This is, of course, only possible at times without significant layers of higher clouds and aerosols. The raw data for this image were extracted from the African Monsoon Multidisciplinary Analysis (AMMA) database with a resolution at nadir of 3 km. The "Night Microphysical" scheme [*Lensky and Rosenfeld*, 2008] uses the same channel combination and is described on the EUMETSAT web page (http://oiswww.eumetsat.int/~idds/html/doc/fog_interpretation.pdf). Here, however, the parameter ranges in the composite were modified slightly to meet tropical conditions: blue: 253 to 313K; red: -4 to +2 K; green: 0 to +3 K. Values lower (higher) than these ranges were set to zero (saturation).

A detailed snapshot on low-level clouds is possible during overpasses of the A-Train satellite constellation [*Stephens et al*., 2002] around 0130 and 1330 LT. As shown in Figure 1c of the main paper, the CALIPSO lidar backscatter coefficient can provide fine detail of low clouds if the atmosphere above is sufficiently clean and cloud free. The data were downloaded from the Langley Atmospheric Science Data Center at http://eosweb.larc.nasa.gov/ PRODOCS/calipso/table_calipso.html. CloudSat 94 GHz reflectivity is much less suited to detect low clouds due to usually small droplets and ground clutter (Figure 1d of the main paper). These data were obtained from the CloudSat Data Processing Center at http://cloudsat.cira.colostate.edu/. The difficulty to observe the extensive nocturnal continental stratus over West Africa discussed here is certainly one of the reasons why it has received so little attention from the scientific community so far.

3. Monitoring of low-level winds

Wind speed away from the surface is currently not observed from space (except of cloud motion winds), so that monitoring relies entirely on radiosondes, pilot balloons, or wind profilers with poor spatial coverage and usually only few observations per day for the former two. During the AMMA Special Observing Period in 2006, four new radiosonde stations were established or re-activated in the Guinea-Soudanian monsoon inflow zone of West Africa. During July–September 2006, launches were performed four-times daily at 0000, 0600, 1200, and 1800 UTC, with additional soundings at 0300, 0900, 1500, and 2100 UTC between 01 and 15 August 2006. The mean high-resolution (about every 5-10 m in the vertical) wind profiles displayed in Figure 2c of the main paper are computed using data from Abuja (Nigeria), Cotonou and Parakou (both Benin), and Tamale (Ghana) (see Figure S1 for locations). Corresponding climatologies of individual stations are shown in Figure S4. Each station shows an early morning wind peak below 1000 m between 0300 and 0900 UTC. This NLLJ is weakest at Abuja at 0300 UTC with about 6 m s^{-1} (likely due to the proximity to the central Nigerian Mountains; Figure S4a) and strongest at the coastal station of Cotonou with mean winds at 0600 UTC in excess of 9 m s^{-1} (Figure S4c). Note the low-level (about 250 m above ground) wind maximum at Parakou and the substantial vertical wind shear in the level underneath it (Figure S4b). Another source of information, which was available in 2006 only, is the UHF profiler data from Djougou shown in Figure 1f of the main paper (see Figure S1 for station location).

4. Monitoring of solar irradiance

(a) Ground-based

Long-term ground-based radiation measurements are not available in southern West Africa. The four stations Ilorin, Parakou, Cotonou, and Kumasi (Owabi) (see Figure S1 for locations) used for the main paper have been or are currently operated in the framework of research projects. Shortwave radiation at a height of two meters above ground is measured at all sites by WMO first or secondary class pyranometers with a temporal resolution of ten minutes or better.

- Ilorin (Nigeria), 8°32'N, 4°34'E, 350 m a.m.s.l.: These measurements are part of the Baseline Surface Radiation Network (BSRN) and are taken in a rural area north of Ilorin covered by shrubs [*Aro*, 2007]. Both short- and longwave radiation is available. The used instrument is a PSP pyranometer from Eppley (WMO first class). The data is available from September 1992 to July 2005, but has several gaps. For this study only years for which the July–September period is fully available are used.
- Parakou (Benin), 9°21'N 2°37'E, 393 m a.m.s.l. and Cotonou (Benin) 6°21'N 2°23'E, 9 m a.m.s.l.: These measurements were carried out at the SYNOP stations located at the airports of Parakou and Cotonou as part of the GLOWA IMPETUS project [*Speth et al.*, 2010]. At least during the wet season, the surface around the stations is covered with grass. Employed instruments are CNR1 net radiometers from Kipp & Zonen (WMO secondary class) that allow the measurement of short- and longwave incoming and outgoing radiation. Data are available from October 2001 to January 2011 for Parakou

and from June 2001 to October 2008 for Cotonou. The July–September period is complete at both stations for all years.

- Kumasi, Owabi, (Ghana), 6°44'N, 1°42'W, 266 m a.m.s.l.: These measurements are taken at the GMET station near the village of Owabi in the rural area northwest of Kumasi as part of the QWeCI project (http://www.liv.ac.uk/qweci/). The surface is covered with grass. The radiation measurements here are part of an automatic weather station. Available parameters are short- and longwave incoming and outgoing radiation, soil heat flux, soil moisture, temperature, humidity and three-dimensional wind. The radiometer is also a CNR1 from Kipp & Zonen. Wind measurements at a temporal resolution of 10 Hz at a height of 4.5 m are taken with an USAT1 ultrasonic anemometer from Metek. The data is available from May 2010 to May 2011 with a complete July–September period 2010.

(b) Satellite products

Surface solar irradiance retrievals from space are based on cloud information derived from satellite measurements. In the main paper only the GEWEX product is shown as an example (Figure 2d). Information on this, the ISCCP radiation data set, and three different surface radiation data sets from the EUMETSAT Satellite Application Facility on Climate Monitoring (CM SAF) is provided below. All but the CMSAF-MVIRI dataset use satellite-derived cloud information as input for a radiative transfer scheme to calculate the surface radiation.

- GEWEX: The radiation dataset of the Global Energy and Water Cycle Experiment (GEWEX-SRB, http://www.gewex.org/srbdata.htm) [*Stackhouse et al.,* 2011] uses cloud information on a 1° x 1° latitude-longitude grid from the ISCCP pixel-level (DX) dataset to derive the solar surface radiation with an algorithm based on *Pinker and Laszlo* [1992]. The dataset includes short- and longwave surface and top-of-the-atmosphere (TOA) radiation fluxes on a 1° x 1° grid as 3-hourly, daily, monthly, as well as 3-hourly and monthly mean products and is available from 1983 to 2007.
- CMSAF-GAC: This dataset is based on satellite measurements from the Advanced Very High Resolution Radiometer (AVHRR) instruments onboard the National Oceanic and Atmospheric Administration (NOAA) satellites and the MetOp-A satellite. Cloud information is derived on a pixel-basis (approx. 5 km) using the Polar Platform System (PPS) software package provided by the Satellite Application Facility on Support to Nowcasting and Very Short Range Forecasting (NWC SAF, http://nwcsaf.inm.es) [*Dybbroe et al*., 2005a; 2005b], which is then used to derive the surface solar radiation on a 0.05° x 0.05° grid with the approach by *Mueller et al*. [2009]. The data is generated as daily and monthly means on a global 0.25° x 0.25° grid for 1989 to 2009.
- CMSAF-MVIRI: The CMSAF-MVIRI solar surface radiation dataset is based on the Meteosat Visible Infra-Red Imager (MVIRI) instruments onboard the geostationary Meteosat First Generation satellites. The retrieval method is based on the Heliosat method [*Cano et al*., 1986; *Hammer et al*., 2003] and uses only information from the visible satellite channel. The dataset ranges from 1983 to 2005 and provides surface solar total and direct irradiance together with the effective cloud index as hourly, daily,

and monthly means at a high spatial resolution (0.03° x 0.03°) for the full disc of the MVIRI instruments. The dataset is freely available in netcdf format from the CM SAF webpage (http://www.cmsaf.eu).

- ISCCP: The radiation dataset of ISCCP (http://isccp.giss.nasa.gov/) is mainly based on the ISCCP-D1 dataset, which provides 3-hourly global information on atmospheric, surface, and cloud properties at a spatial resolution of 280 km between 1983 and 2007 [*Rossow and Schiffer*, 1999]. The radiation dataset (called ISCCP-FD) provides full- and clear-sky, short- and longwave, upwelling and downwelling radiation fluxes at the TOA and the surface as well as on three atmospheric levels at the same spatial and temporal resolution as the ISCCP-D1 dataset [*Zhang et al.*, 2004].
- CMSAF-SEVIRI: This dataset is based on cloud properties derived by the Nowcasting-Algorithm applied to the measurements from the SEVIRI instruments onboard the MSG satellites [*Derrien and Le Gléau*, 2005]. The calculation of the surface radiation based on the cloud information is conducted on a pixel-level (approx. 3 km) using the algorithm described in *Mueller et al.* [2009]. The final products are available in daily, 1-hourly monthly, and monthly means from 2007 (European coverage starting already in 2005) until present from the CM SAF webpage (http://www.cmsaf.eu).

(c) Comparison between different products

Figure S5 shows climatologies for the four satellite products introduced in the previous subsection, which should be compared with Figure 2d of the main paper for GEWEX (note the different time periods used for averaging here). All five products agree in terms of the large-scale structure with a local minimum over southern West Africa straddled by higher insolation over the Sahel and the eastern tropical Atlantic. While agreement over the ocean is large, the products deviate more strongly over land with very low values in the CMSAF-GAC product over the Sahel for example. Averaged over the box indicated in the plots (also used in the main paper) the different products tend to show a slight positive bias with respect to GEWEX, ERA-Interim, and the station observations, which is most pronounced in ISCCP and CMSAF-MVIRI (Figures S5b and S5c).

Time series of July–September means spatially averaged over the box show that these biases are systematic and dominate over the interannual variability, which shows some coherence between the products (Figure S6). The station observations also show a fairly large interannual variability that is not always matched by the regionally averaged satellite products (e.g., the sunny year 2003 at Cotonou). Interestingly the ERA-Interim re-analysis data (see Section 5) show a positive trend, which is not evident from any other source of information. It is not clear, whether this trend is an atmospheric signal or a result of changes to the data assimilated to generate the re-analysis.

For a fairer comparison, Table S1 shows values from the satellite products and ERA-Interim from the gridpoint nearest to the available observing stations and averaged over the same time period. The results confirm the clear positive bias in ISCCP and CMSAF-MVIRI, but show satisfactory agreement for CMSAF-GAC and GEWEX with slightly higher values for CMSAF-SEVIRI. ERA-Interim tends to underestimate the station observations, potentially due to the low radiation values at the beginning of the time series in the ERA-Interim dataset (see Figure S6).

5. Gridded model datasets

(a) ERA-Interim short-term forecasts

As a near-observational modeling reference, short-term forecasts started at 0000 UTC every day made in the production of the European Centre for Medium-Range Weather Forecasts (ECMWF) ERA Interim re-analyses [*Dee et al*., 2011] covering the period 1989–2010 have been used throughout the main paper (see Figure 3). The advantages of using short-term forecasts are (i) a 3-hourly time resolution (in contrast to 6-hourly for the actual re-analysis data) and (ii) a physically consistent diurnal cycle using the model forecast times +3h to +24h. Since solar irradiance data are not assimilated, differences between short-term model forecasts and the actual re-analysis are small (not shown).

Native resolution of the ERA-Interim model is T255L60. For this study the data were interpolated to a 0.5° latitude-longitude grid and pressure levels 1000, 975, 950, 925, 900, 875, 850, 825, 800, 775, 750, 700, 650, 600, and 500 hPa. Considered parameters are daily averaged surface solar radiation downwards, low cloud cover (defined as below 0.8 times the surface pressure), layer cloud cover as well as zonal and meridional wind. Daily mean wind speeds have been computed in two ways: (i) calculate wind speed for each 3-hourly value and then a long-term mean (solid line in Figure 3c in the main paper), (ii) calculate wind speed from mean zonal and meridional wind for each day and then compute a long-term mean (solid line in Figure 4b). The latter is slightly smaller due to the cancellation of positive and negative contributions during the day, but matches with the averaging procedure used by most CMIP3 models (see next subsection).

(b) CMIP3 multi-model dataset

The data used to generate Figure 4 of the main paper are from the the World Climate Research Programme's (WCRP's) Coupled Model Intercomparison Project phase 3 (CMIP3) multi-model dataset [*Meehl et al.,* 2007], which formed the basis for the Fourth Assessment Report from the Intergovernmental Panel on Climate Change (IPCC). The data were downloaded from the ftp server of the WCRP's Working Group on Coupled Modeling (WGCM) hosted at the Lawrence Livermore National Laboratory, Livermore, CA, USA. Details on the participating models and definitions of model variables can be found at http://www-pcmdi.llnl.gov/ipcc/about_ipcc.php. A summary of the data used here is given in Table S2. The focus of this study is on the "climate of the 20th Century experiments (20C3M)", which were initialized in the pre-industrial control runs. The period 1961–1999 was chosen for two reasons: (i) it is long enough to represent the models' background climate states and (ii) both daily and monthly averages are available. For such an extended period differences between means over single runs of a given model were almost indistinguishable, so that only one run is considered (run 1 for most models). From the 24 models listed on the webpage given above a 20-model ensemble was created in the following way: (i) output from CCCMA CGCM3.1(T47) and CCCMA CGCM3.1(T63), GFDL-CM2.0 and GFDL-CM2.1, and GISS-EH and GISS-ER were too similar to be regarded as independent and were therefore averaged; (ii) CSIRO-Mk3.0 and CSIRO-Mk3.5 did produce significantly different results, but it was decided to include the most recent version of the model only that showed much more realistic fields over West Africa.

Parameters considered here are monthly means of surface downwelling shortwave flux in air (rsds) in W m^{-2} and cloud area fraction in atmospheric layer (cl) in % given on model levels, as well as both daily and monthly means of the eastward (ua) and northward wind (va) component in m s^{-1} given on the standard pressure levels 1000, 925, 980, 700, 600, and 500 hPa. Table S2 provides summer mean, regionally averaged values of rsds for the 19 models that provide data for this parameter. As discussed in the main paper the model differences are substantial, reaching from 144.8 to 257.1 W m^{-2} with six models underestimating and 13 overestimating with respect to ERA-Interim data. This gives a mean of 190.2 W m^{-2} with a standard deviation of 39.4 W m^{-2}. For all models differences to ERA-Interim are statistical significant on at least the 95% level. These differences are much larger than differences between 20C3M and the atmosphere-only experiment AMIP (1980–1997; only 13 models available) or the SRESA1B scenario (2050–2099; all 19 models available) for individual models (Figure S7).

In order to make the cloud information comparable, the time-mean, area-averaged surface pressure was used to convert from model levels to pressure levels. Strictly, this should be done for each gridpoint and time step separately and then interpolated onto a common vertical grid, but given that there is no significant orography in the study area (see Figure S1) and that month-to-month pressure difference during summer are very small, the introduced error should be negligible. Wind speed was computed as the square root of the sum of the squares of the zonal and meridional components. Ideally this should be computed with instantaneous data to better match with radiosonde and ERA-Interim re-analyses. Here daily means were used for all models that provide those. For these models a comparison between daily and monthly means revealed typical differences in wind speed at 925 hPa of 0.5 m s^{-1} due to cancellation of positive and negative values within a given month. For the four models that did not provide daily output, monthly data were used instead and marked accordingly in Figure 4b. Estimates from these models should therefore be regarded as upper bounds, which points to an even larger wind bias in the CMIP3 models as a whole.

(c) Regridding procedure

All regional averages used in this paper refer to the region 6–10°N, 7°W–7°E that represents the core of the West Africa stratus belt (see black boxes in Figure S5 for example). As neither ERA-Interim nor the CMIP3 data is available on an adequate grid for this box choice, all fields had to be remapped before spatial averages could be computed. To do this, the first-order conservative remapping routine implemented in the Climate Data Operator (CDO) software package [*Schulzweida et al*., 2011] was used as described in *Jones et al*. [1999]. The target grid is a simple 1° latitude by 1° longitude grid with grid box centre points located in the middle between two latitude/longitude circles (4 by 14 grid points over the region of interest). Wind speed was calculated from the zonal and meridional components before the regridding was applied. Clearly, the coarse resolution of some of the CMIP3 models describe above will introduce some error, since information from relatively far away is included in the box average. At least the conservative remapping ensures that grid boxes that belong only partially to the target box are weighted accordingly.

Acknowledgments

We would like to acknowledge the Meteorological services of Ghana and Benin for providing SYNOP information to generate Figure S2. The generation of the CM SAF data sets has been funded by EUMETSAT in the context of the Climate Monitoring (CM SAF) part of the Satellite Application Facilities Network. The ISCCP Surface Radiation data were obtained from ftp://isccp.giss.nasa.gov/outgoing/FLUX.

References

Aro, T. O. (2007), *Horizon at station Ilorin*, Department of Physics, University of Ilorin, Ilorin, Nigeria, doi:10.1594/PANGAEA.669517.

Cano, D., J. M. Monget, M. Albuisson, H. Guillard, N. Regas, and L. Wald (1986), A method for the determination of the global solar radiation from meteorological satellite data, *Solar Energy, 37,* 31–39.

Dee, D. P., et al. (2011), The ERA-Interim reanalysis: configuration and performance of the data assimilation system, *Q. J. R. Meteorol. Soc., 137,* 553–597.

Derrien, M., and H. Le Gléau (2005), MSG/SEVIRI cloud mask and type from SAFNWC, *Int. J. Rem. Sens., 26(21),* 4707–4732.

Dybbroe, A., K.-G. Karlsson, and A. Thoss (2005a), NWCSAF AVHRR cloud detection and analysis using dynamic thresholds and radiative transfer modelling. Part I: Algorithm description, *J. Appl. Meteorol., 44,* 39–54.

Dybbroe, A., K.-G. Karlsson, and A. Thoss (2005b), NWCSAF AVHRR cloud detection and analysis using dynamic thresholds and radiative transfer modelling. Part II: Tuning and validation, *J. Appl. Meteorol., 44,* 55–71.

Hammer, A., D. Heinemann, C. Hoyer , R. Kuhlemann, E. Lorenz, R. Müller, and H. G. Beyer (2003), Solar energy assessment using remote sensing technologies, *Rem. Sens. Env., 86,* 423–432.

Jones, P. W. (1999), First and second order conservative remapping schemes for grids in spherical coordinates, *Mon. Wea. Rev., 127,* 2204–2210.

Lensky, I. M., and D. Rosenfeld (2008), Clouds-aerosols-precipitation satellite analysis tool (CAPSAT), *Atmos. Chem. Phys., 8,* 6739–6753.

Meehl, G. A., C. Covey, T. Delworth, M. Latif, B. McAvaney, J. F. B. Mitchell, R. J. Stouffer, and K. E. Taylor (2007), The WCRP CMIP3 multi-model dataset: A new era in climate change research, *Bull. Am. Meteorol. Soc., 88,* 1383–1394.

Mueller, R. W., C. Matsoukas, A. Gratzki, H. D. Behr, and R. Hollmann (2009), The CM-SAF operational scheme for the satellite based retrieval of solar surface irradiance – A LUT based eigenvector hybrid approach, *Rem. Sens. Env., 113,* 1012–1024.

Pinker, R. T., and I. Laszlo (1992), Modelling surface solar irradiance for satellite applications on a global scale, *J. Appl. Meteorol., 31,* 194–211.

Rossow, W. B., and R. A. Schiffer (1999), Advances in understanding clouds from ISCCP, *Bull. Am. Meteorol. Soc., 80,* 2261–2288.

Schulzweida, U., L. Kornblueh, and R. Quast, R. (2011), *Climate Data Operators, Version 1.5.0.* Max-Planck Institute for Meteorology, Hamburg, Germany, available online https://code.zmaw.de/projects/cdo/wiki/Cdo.

Speth, P., *et al.* (2010), *Impacts of global change and the hydrological cycle in West and Northwest Africa*, Springer, Berlin, Germany, doi: 10.1007/978-3-642-12957-5.

Stackhouse Jr., P. W., S. K. Gupta, S. J. Cox, T. Zhang, J. C. Mikovitz, and L. M. Hinkelman (2011), 24.5-year SRB data set released, *GEWEX News, 21(1),* 10–12.

Stephens, G., et al. (2002), The Cloudsat mission and the A-train, *Bull. Am. Meteorol. Soc., 83,* 1771–1790.

World Meteorological Organization (1995), *Manual on codes. International Codes, Vol. I.1, Part A—Alphanumeric Codes.* WMO-No. 306, World Meteorological Organization, Geneva, Switzerland.

Zhang, Y., W. B. Rossow, A. A. Lacis, V. Oinas, and M. I. Mishchenko (2004), Calculation of radiative fluxes from the surface to top of atmosphere based on ISCCP and other global datasets: Refinements of the radiative transfer model and the input data, *J. Geophys. Res., 109,* D19105, doi:10.1029/2003JD004457.

Figures & Tables

	Obs	ERA	ISCCP	GEWEX	CMSAF-MVIRI	CMSAF-GAC	CMSAF-SEVIRI
Ilorin	170	164	200	173	200	169	181
Cotonou	198	169	198	183	210	199	198
Parakou	177	169	208	183	202	172	183
Kumasi	147	164	197	167	191	166	173

Table S1. Comparison between ground and space-based observations of solar irradiance at the surface. The 2nd column gives summer mean (July–September) values (in W m^{-2}) at four observing stations in West Africa (see Figure S1 for locations). Averaging time periods correspond to the data availability of the stations (see Figure S6). The six following columns give corresponding time averages from the nearest gridpoint of the ERA re-analysis (see Section 5) and five satellite products (see Section 4b).

Model name	ua & va	cl	rsds	Remark	mean rsds
BCCR-BCM2.0	d & m	m	m		144.8**
CCCMA CGCM3.1	d & m	m	m	mean of T47 & T63	166.9*
CNRM-CM3	d & m		m		149.9**
CSIRO-Mk3.5	d & m	m	m		200.0**
GFDL_CM2	d & m	m	m	mean of versions 1 & 2	169.4*
GISS-AOM	d & m		m	ua and va on different grids	259.0**
GISS-E	d & m	m	m	mean of versions E & H	214.0**
IAP FGOALS1-g1.0	d & m	m	m		228.9**
INGV_SXG	d & m	m			
INM-CM3.0	d & m	m	m		159.3**
IPSL-CM4	d & m	m	m		251.9**
MIROC3.2(hires)	d & m	m	m		176.4**
MIROC3.2(medres)	d & m	m	m		149.8**
MIUB ECHO-G	d		m		151.4**
MPI ECHAM5	d & m	m	m		154.9**
MRI-CGCM2.3.2	d & m	m	m		257.1**
NCAR CCSM3	m	m	m		178.3**
NCAR PCM	m	m	m		177.9**
UKMO-HadCM3	m	m	m		186.1**
UKMO-HadGEM1	m		m		237.6**

Table S2. Availability of CMIP3 data. List refers to the period from 1961 to 1999 from the 20C3M experiments. 'm' stands for monthly data and 'd' for daily. The meanings of the variables are given in the text. The last column gives July–September rsds averages in W m^{-2} over the target box 6–10°N, 7°W–7°E. * and ** indicate statistical significance of the difference to the ERA-Interim data on the 95%- and 99% level, respectively, based on a two-sided Welch's t-test.

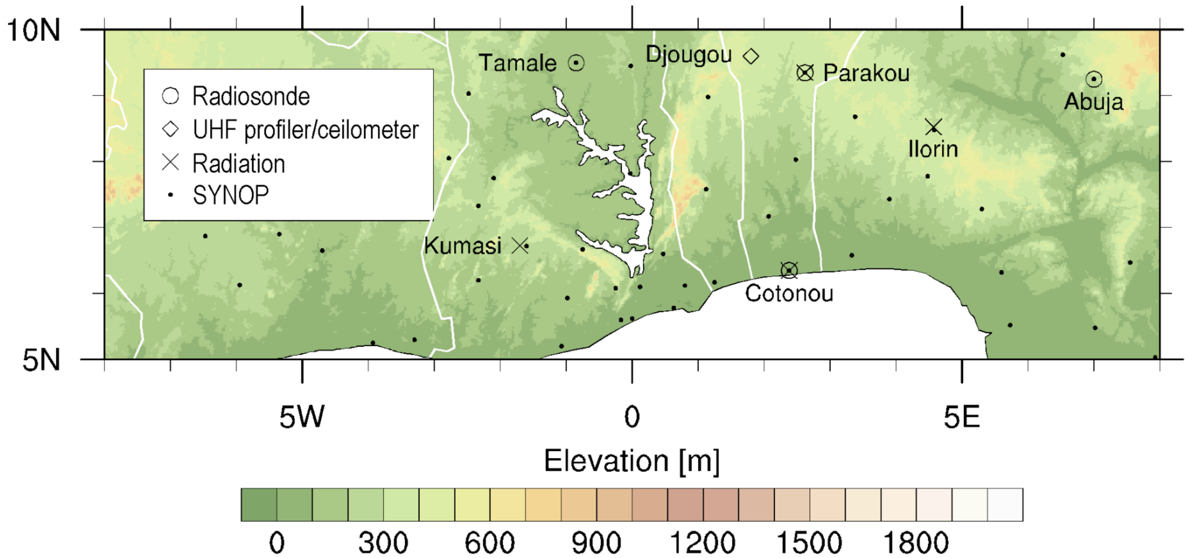

Figure S1. Map of southern West Africa showing elevation (color shading) and the location of the sites for ground-based observations used in the main paper and the Auxiliary Material. The site of the UHF profiler and the ceilometer used for Figures 1e and 1f of the main paper is referred to as Nangatchori in other publications, which is about 10 km away from Djougou.

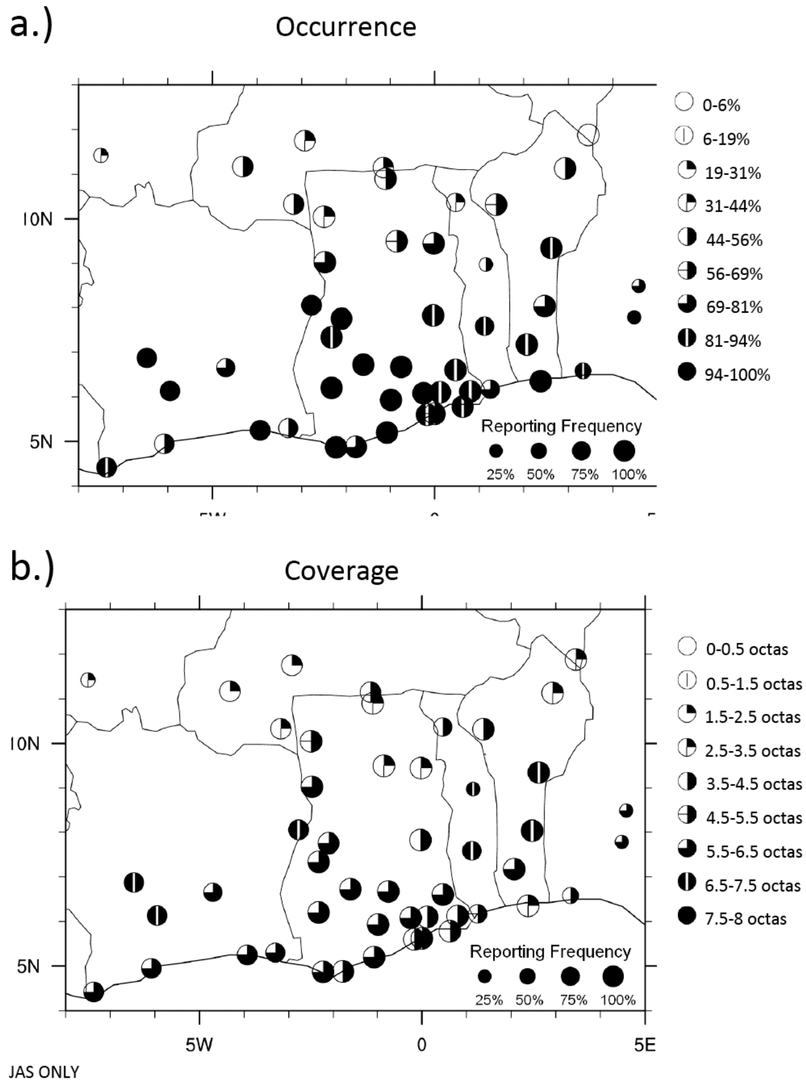

Figure S2. Human-eye observations of low-level stratus and stratocumulus clouds. (**a**) Frequency of occurrence and (**b**) average coverage during July–September 2006 at 0600 UTC. The size of the marker indicates the frequency of station reports.

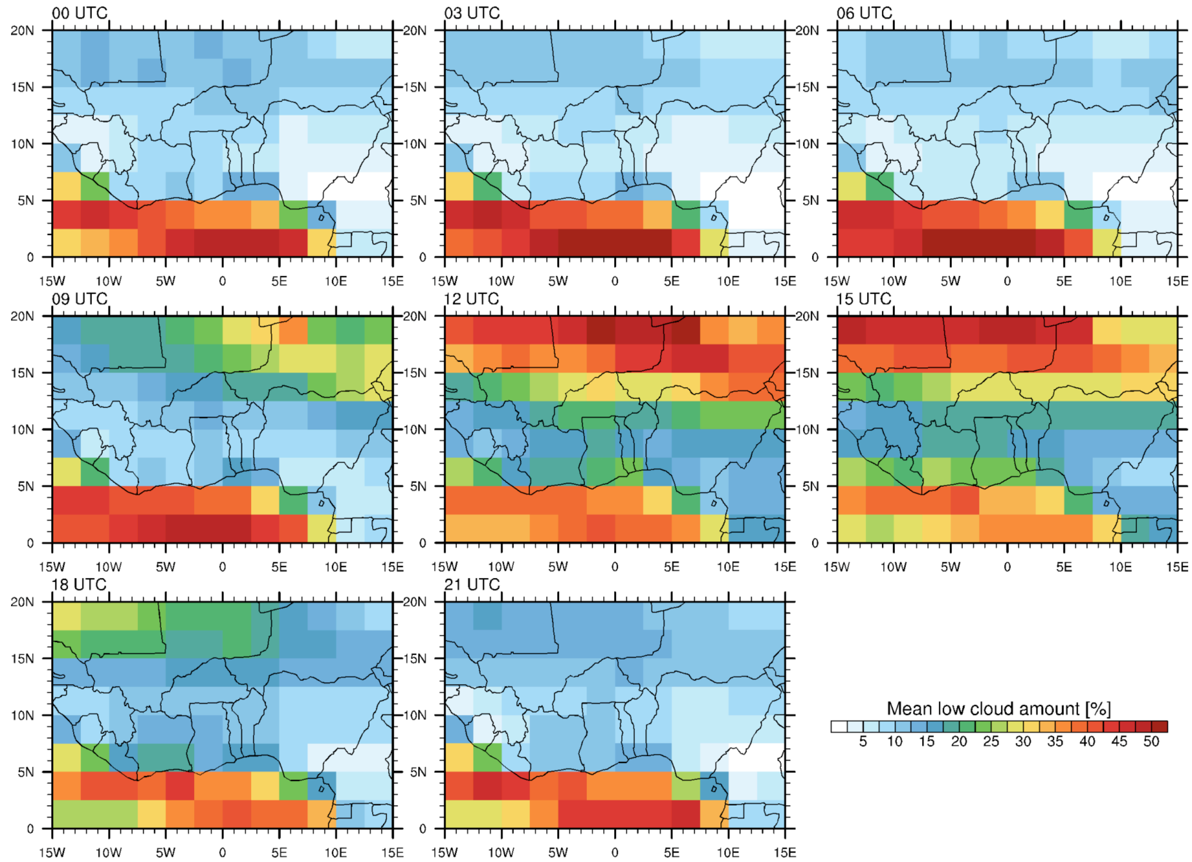

Figure S3. Diurnal cycle of low-cloud cover from ISCCP D2. Shown is the summer mean (July–September) for the period 1983–2007.

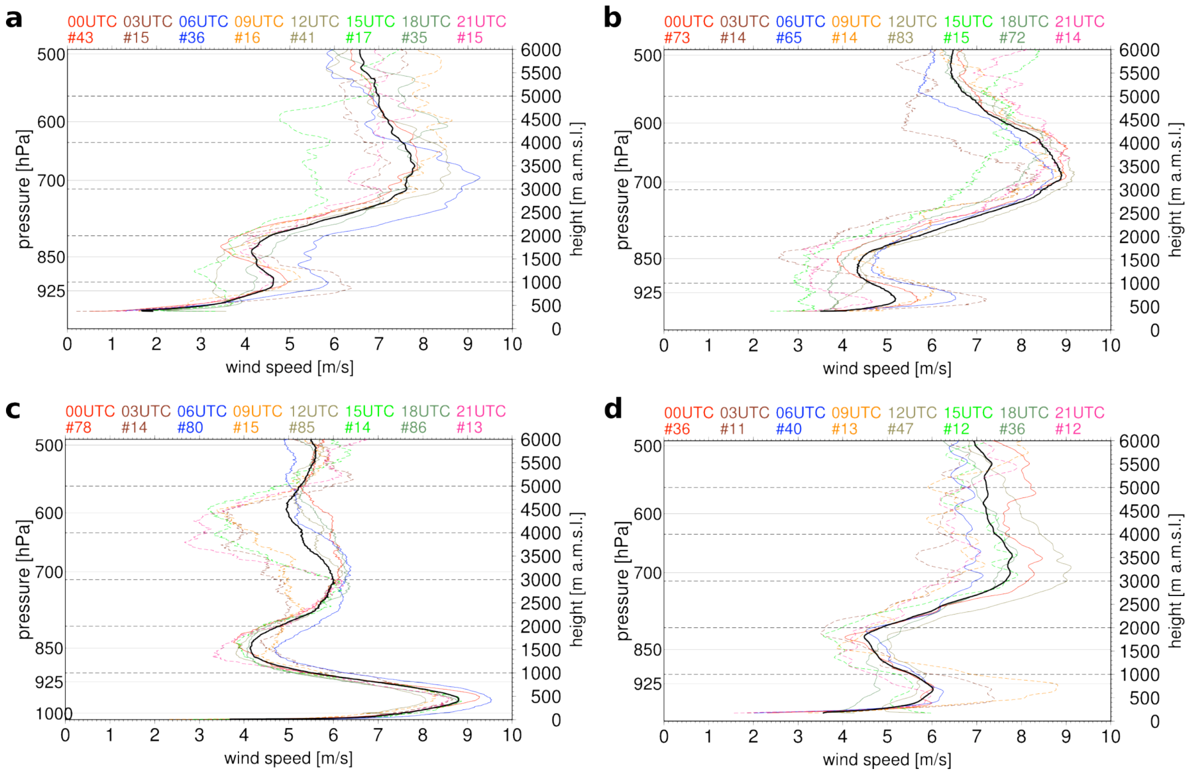

Figure S4. Diurnal cycle of vertical profiles of wind speed. The three-hourly means are calculated from radiosondes at (a) Abuja (Nigeria, WMO number 65125), (b) Parakou (Benin, WMO number 65330), (c) Cotonou (Benin, WMO number 65344), and (d) Tamale (Ghana, WMO number 65418) (see Figure S1 for locations) for July–September 2006. The black line is the daily average. The numbers below the time at the top of the panels denote the number of soundings that were used for the averaging.

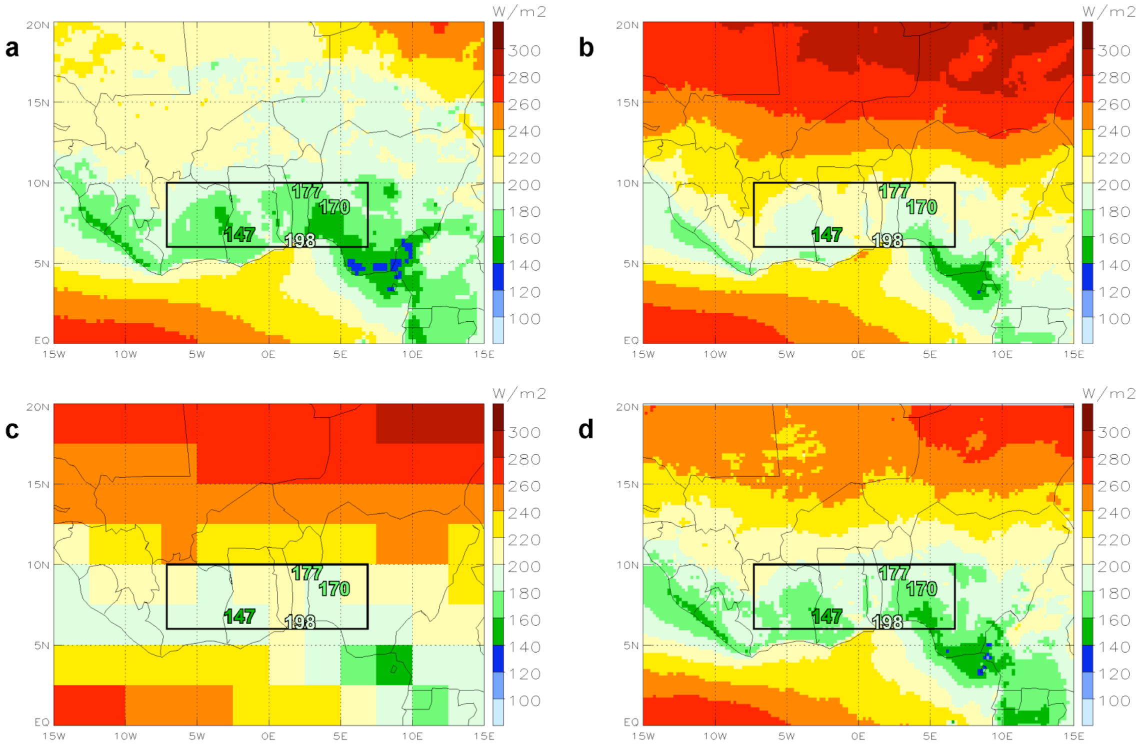

Figure S5. Satellite estimates of solar irradiance at the surface. Shown are summer mean (July–September) values in W m^{-2} from (a) CMSAF-GAC 1989–2009, (b) CMSAF-MVIRI 1989–2005, (c) ISCCP 1983–2007, and (d) CMSAF-SEVIRI 2007–2010 (see Section 4b). Observations from the four ground stations Ilorin (Nigeria), Cotonou, and Parakou (Benin), and Kumasi (Ghana) (see Figure S1 for locations) are included as numbers (see Section 4a). The black boxes in all panels mark the area used for spatial averaging throughout this paper (6–10°N, 7°W–7°E).

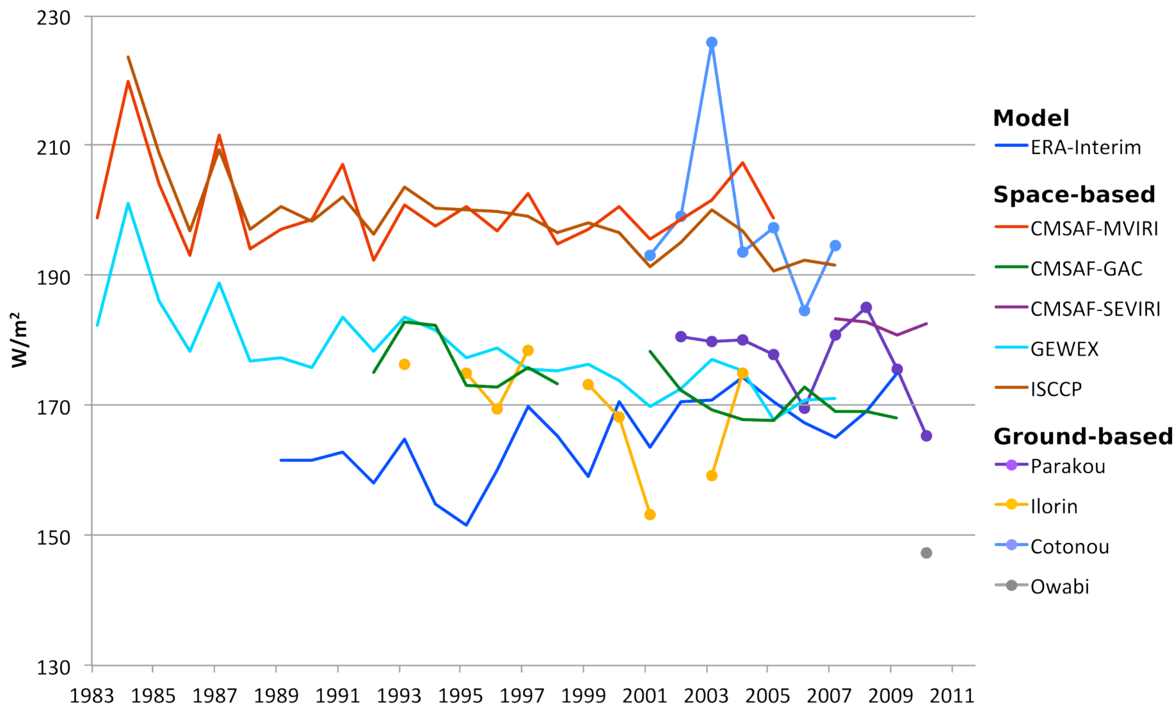

420

421

422 **Figure S6.** Time series of solar irradiance at the surface. Shown values are summer means

423 (July–September) in W m^{-2} from different satellite products (see Section 4b) and from

424 ERA-Interim short-term forecasts (see Section 5a) all averaged over the box 6–10°N, 7°W–

425 7°E, as well as from the four ground-based pyranometers at Ilorin (Nigeria), Cotonou, and

426 Parakou (Benin), and Kumasi (Ghana) all located within this box (see Section 4a). The

427 locations of the stations are marked in Figure S1.

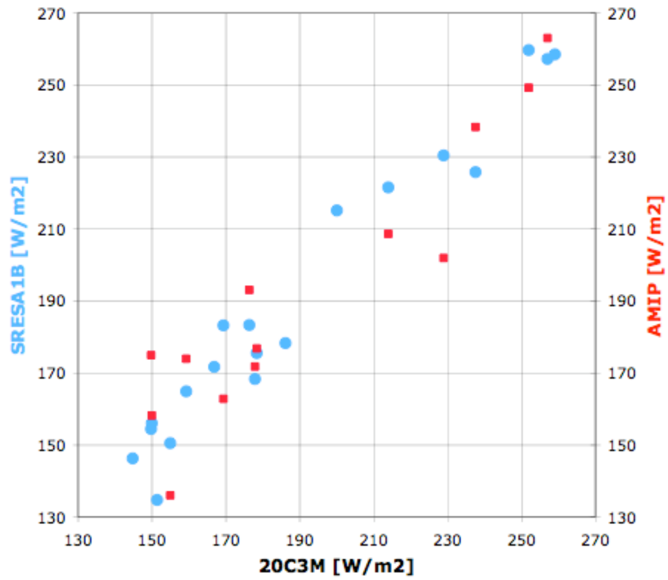

Figure S7. Comparison of solar irradiance between different CMIP3 models and experiments/time periods. All values are regionally averaged July–September means in W m^{-2}. Bottom axis: 20C3M experiment 1961–1999 as in Figure 4 of the main paper; right axis: atmosphere-only experiment AMIP 1980–1997 (13 models available only); left axis: SRESA1B scenario 2050–2099. The scatter plot is clearly dominated by the differences between single models rather than experiments/time periods.